

The shape of dark matter subhalos in the Aquarius simulations

Carlos A. Vera-Ciro^{1,2*}, Laura V. Sales³, Amina Helmi² and Julio F. Navarro⁴

¹ Department of Astronomy, University of Wisconsin, 2535 Sterling Hall, 475 N. Charter Street, Madison, WI 53076, USA

² Kapteyn Astronomical Institute, University of Groningen, PO Box 800, 9700 AV Groningen, The Netherlands

³ Max-Planck-Institut für Astrophysik, Karl-Schwarzschild-Straße, 1, 85740 Garching bei München, Germany

⁴ Senior CIFAR Fellow. Department of Physics & Astronomy, University of Victoria, Victoria, BC, V8P 5C2, Canada

16 October 2018

ABSTRACT

We analyze the Aquarius simulations to characterize the shape of dark matter halos with peak circular velocity in the range $8 < V_{\max} < 200$ km/s, and perform a convergence study using the various Aquarius resolution levels. For the converged objects, we determine the principal axis ($a \geq b \geq c$) of the normalized inertia tensor as a function of radius. We find that the triaxiality of field halos is an increasing function of halo mass, so that the smallest halos in our sample are $\sim 40 - 50\%$ rounder than Milky Way-like objects at the radius where the circular velocity peaks, r_{\max} . We find that the distribution of subhalo axis ratios is consistent with that of field halos of comparable V_{\max} . Inner and outer contours within each object are well aligned, with the major axis preferentially pointing in the radial direction for subhalos closest to the center of their host halo. We also analyze the dynamical structure of subhalos likely to host luminous satellites comparable to the classical dwarf spheroidals in the Local Group. These halos have axis ratios that increase with radius, and which are mildly triaxial with $\langle b/a \rangle \sim 0.75$ and $\langle c/a \rangle \sim 0.60$ at $r \sim 1$ kpc. Their velocity ellipsoid become strongly tangentially biased in the outskirts as a consequence of tidal stripping.

Key words: methods: numerical - galaxies: dwarf - cosmology: dark matter.

1 INTRODUCTION

In the Λ cold dark matter cosmological paradigm structures build hierarchically, via the mergers of smaller objects (Press & Schechter 1974; Gott & Rees 1975; White & Rees 1978; Blumenthal et al. 1984). As mergers proceed, the innermost regions of some of the progenitors survive, resulting in non-linear structures where a wealth of substructure orbits the center of an otherwise monolithic dark halo. Early N -body simulations showed that halos could host dozens of substructures, down to masses near the numerical resolution limit (Tormen 1997; Tormen, Diaferio & Syer 1998; Ghigna et al. 1998; Klypin et al. 1999a,b; Moore et al. 1999). For systems like the Milky Way, current numerical simulations have extended the dynamical range of resolved substructures by 4-5

orders of magnitude (Diemand, Kuhlen & Madau 2007; Diemand et al. 2008; Springel et al. 2008; Stadel et al. 2009).

The properties of these substructures are of great interest since luminous satellites, such as the population of dwarf spheroidal (dSph) galaxies in the Local Group, are expected to be embedded in them (Stoehr et al. 2002; Strigari et al. 2007; Boylan-Kolchin, Bullock & Kaplinghat 2012; Vera-Ciro et al. 2013). Furthermore, the large mass-to-light ratios of dSph, which range from 10 s to 1000 s (Mateo 1998; Gilmore et al. 2007; Walker 2013), indicate that their internal dynamics is dominated by the dark matter. This suggests that the predictions of pure dark matter simulations may be directly confronted with observations of these systems. For instance, it has been suggested that they provide an optimal place to look for signals of dark matter self-annihilation processes (Kamionkowski, Koushiappas & Kuhlen 2010) due to the natural enhancement in density and the lack of significant contamination from the baryonic component.

The availability of large samples of line-of-sight veloc-

* E-mail: ciro@astro.wisc.edu

ities for individual stars in dSph galaxies offers new tests of the predictions of Λ cold dark matter (Λ CDM) regarding the structure of dark matter subhalos. For instance, studies of N -body numerical simulations have shown that the inner slope of the dark matter density profile is expected to be cuspy in CDM models (Navarro, Frenk & White 1996, 1997). This seems to contrast with the somewhat shallower slopes and even constant density cores proposed to explain the motions of stars in local dwarf spheroidals (Amorisco & Evans 2011; Walker & Peñarrubia 2011; Amorisco & Evans 2012; Jardel & Gebhardt 2012). This, however, is a subject of active debate, since various authors have shown that the stellar kinematics of Milky Way dwarfs are also consistent with the NFW cuspy profiles (Battaglia et al. 2008; Walker et al. 2009; Strigari, Frenk & White 2010; Breddels et al. 2013; Breddels & Helmi 2013).

Most of the dynamical modeling performed in the studies of Local Group dwarf spheroidals relies on simple assumptions about the structure of their dark matter component. In particular, spherical symmetry and specific anisotropy profiles have been extensively assumed. The orbital anisotropy has been taken to be constant (Richstone & Tremaine 1986; Lokas 2002; Lokas, Mamon & Prada 2005; Lokas 2009; Walker et al. 2009), or radially dependent (Kleyna et al. 2001; Wilkinson et al. 2002; Battaglia et al. 2008; Strigari et al. 2008; Wolf et al. 2010; Amorisco & Evans 2011), while in Schwarzschild modeling or in made-to-measure N -body methods it does not need to be assumed (Long & Mao 2010; Jardel & Gebhardt 2012; Breddels et al. 2013). The selection of geometric shape for the dark matter potential can also be relaxed. For example, Hayashi & Chiba (2012) considered axisymmetric dark matter halos to model some of the Milky Way dSph galaxies.

For isolated galaxies, numerical experiments of Λ CDM have clear predictions for these quantities. The shapes of (isolated) dark matter halos in the mass range $10^{10} - 10^{15} M_{\odot}$, are generally found to be triaxial, with axis ratios depending on the mass of the object (Frenk et al. 1988; Dubinski & Carlberg 1991; Warren et al. 1992; Cole & Lacey 1996; Thomas et al. 1998; Jing & Suto 2002; Bailin & Steinmetz 2005; Kasun & Evrard 2005; Hopkins, Bahcall & Bode 2005; Allgood et al. 2006; Bett et al. 2007; Hayashi, Navarro & Springel 2007; Kuhlen, Diemand & Madau 2007; Stadel et al. 2009; Diemand & Moore 2011; Muñoz-Cuertas et al. 2011; Schneider, Frenk & Cole 2012). In terms of their internal kinematics, the velocity ellipsoid is close to isotropic near the center of halos and becomes mildly radial towards the outskirts (Wojtak et al. 2005; Hansen & Moore 2006; Ludlow et al. 2011).

For subhalos, however, less is known because of the demanding numerical resolution needed to model properly low mass halos orbiting within hosts of Milky Way mass. This situation has recently improved with simulations that are now able to successfully sample the mass function on these scales, such as the Via Lactea, CLUES, GHALO and Aquarius simulations (Diemand, Kuhlen & Madau 2007; Diemand et al. 2008; Springel et al. 2008; Stadel et al. 2009; Libeskind et al. 2010). For instance, using the Via Lactea simulations Kuhlen, Diemand & Madau (2007) found that subhalos are also not spherical, although the effect of tides tends to make subhalos rounder than comparable objects in the field. These results prompt questions about the validity of some of the

assumptions involved in the mass modeling of stellar kinematics in dwarfs. And although the orbital anisotropy of the stars in a dSph is likely unrelated to that of dark matter (and associated to the formation history), it is nonetheless valuable to explore the dynamical structure of subhalos because they provide the main potential.

A detailed study of the shape of the Milky Way mass Aquarius halos was presented in Vera-Ciro et al. (2011). Here we extend this analysis to lower mass objects, both subhalos of the main central halo and field halos, up to $1.5h^{-1}$ Mpc from the center of the main Aquarius halo. The paper is organized as follows. In Section 2 we describe the numerical simulations, introduce the methods we use to determine halo shapes and explore the convergence of the results. In Section 3 we compare the properties of subhalos and isolated objects of similar mass. We analyze subhalo shapes in the context of the kinematic modeling of dwarfs around the Milky Way in Section 4 and summarize our main results in Section 5.

2 SHAPE MEASUREMENTS AND CONVERGENCE

We use the suite of cosmological N -body simulations from the Aquarius project (Springel et al. 2008). These consist of six $\sim 10^{12} M_{\odot}$ Λ CDM halos (Aq-A to Aq-F), re-simulated with five different levels of resolution within the cosmology $\Omega_0 = 0.25$, $\Omega_{\Lambda} = 0.75$, $H = 100h$ km s $^{-1}$ Mpc $^{-1}$, $h = 0.75$. The simulations use the zoom-in technique, with a high-resolution region that extends at $z = 0$ up to $\sim 2 h^{-1}$ Mpc from the center of each main halo. This exceeds the typical virial radius of the Aquarius halos by 5–10 times and allows us to identify isolated halos that have been unaffected by tidal forces (see Springel et al. 2008, for further details).

In most of the analysis that follows we focus on the level-2 resolution runs, with a mass per particle $m_p \approx 10^4 M_{\odot}$. However, we use the other Aquarius levels to test the convergence of our results. Halos and subhalos are identified using the SUBFIND algorithm (Springel et al. 2001). We keep all structures identified with at least 20 particles. We will call the central subhalo of a group a *field/isolated halo*. In this work we consider field halos up to a distance of $1.5h^{-1}$ Mpc from the center of the main Aquarius halo, to avoid contamination of low-resolution particles.

To measure the shape of halos in the simulations we follow the same approach as Vera-Ciro et al. (2011) and iteratively compute the inertia tensor in ellipsoidal regions. At a given radius, the algorithm begins with a spherical contour which is reshaped and reoriented according to the principal axis of the normalized inertia tensor for the encompassed material, until convergence is reached (Allgood et al. 2006). More specifically, we define the normalized inertia tensor as

$$I_{ij} = \sum_{\mathbf{x}_k \in V} \frac{x_k^{(i)} x_k^{(j)}}{d_k^2}, \quad (1)$$

where d_k is a distance measure to the k -th particle and V is the set of particles of interest. Representing dark matter halos as ellipsoids of axis lengths $a \geq b \geq c$, the axis ratios $q = b/a$ and $s = c/a$ are the ratios of the square-roots of the eigenvalues of \mathbf{I} , and the directions of the principal axes are given by the corresponding eigenvectors. Initially, the set V

is given by all particles located inside a sphere which is reshaped iteratively using the eigenvalues of \mathbf{I} . The distance measure used is $d_k^2 = x_k^2 + y_k^2/q^2 + z_k^2/s^2$, where q and s are updated in each iteration. In practice we find that the algorithm converges (i.e. the variation in the shape between successive iterations is $< 1\%$) when there are as few as 200 particles in set V . Notice that this is a more stringent criteria than required by plain identification of bound objects in SUBFIND, which is here taken to be only 20 particles.

In Vera-Ciro et al. (2011) we showed that shapes can be robustly measured from the *convergence radius*, r_{conv} outwards (Power et al. 2003; Navarro et al. 2010). r_{conv} is defined so that the ratio between the local relaxation time and the dynamical time at the virial radius equals κ where:

$$\kappa(r) = \frac{\sqrt{200}}{8} \frac{N(r)}{\ln N(r)} \left[\frac{\bar{\rho}(r)}{\rho_c} \right]^{-1/2}, \quad (2)$$

where $N(r)$ is the number of particles inside the radius r , $\bar{\rho}$ is the spherically averaged density and ρ_c the critical density. We adopt the value $\kappa = 7$ because this guarantees that the circular velocity profiles of the main halos are accurate to better than 2.5% (Navarro et al. 2010). Note that this equation has to be numerically solved for r_{conv} with fixed κ for each object in the simulation. As a rule-of-thumb, we find that requiring a minimum of ~ 10000 particles enclosed within the radius of interest (i.e. r_{max} or r_{95}) ensures that more than 90% of the subhalos satisfy this constraint.

Fig. 1 shows that the same criteria applied to our sample of subhalos also ensure convergence of halo shape estimates. We compare the results for the Aq-A run in all resolution levels 1–5 (red to black, respectively). The left panels show, as a function of halo maximum circular velocity V_{max} , the mean axis ratios computed at r_{95} , here defined as the ellipsoidal contour enclosing the 95% most bound particles identified by SUBFIND. The thin lines correspond to the entire sample of subhalos, whereas the thick curve shows only “converged” objects (those where $r_{95} \geq r_{\text{conv}}$). At level 2, the one used for most of our analysis, the mean axis ratios agree with the highest resolution run Aq-A-1 to better than 5% across the full spectrum of “converged” subhalos.

A similar conclusion is reached for the inner regions of subhalos, as shown by the right panels of Fig. 1. Here, c/a and b/a are computed at the radius of the peak circular velocity V_{max} , which is typically approximately nine times smaller than r_{vir} for field halos and approximately six times smaller than r_{95} for subhalos. The number of objects for which $r_{\text{conv}} < r_{\text{max}}$ is roughly ten times lower than those with $r_{\text{conv}} < r_{95}$. This explains the relatively more noisy behavior of the curves on the right column compared to those on the left (especially for the lowest two resolution runs, where typically less than ten objects satisfy the convergence condition). In general, a subhalo whose shape has converged at the r_{95} radius has not necessarily converged at the r_{max} radius.

Besides the mean trends shown in Fig. 1, we have also explored the convergence of halo shapes on an object-by-object basis. In order to do this, we identify the same subhalos in several resolution levels of the Aq-A halo by matching the Lagrangian positions of all the particles assigned to a substructure by SUBFIND back in the initial conditions (see Section 4.2 Springel et al. 2008, for further details). In addition to this criterion, we impose a maximum deviation on

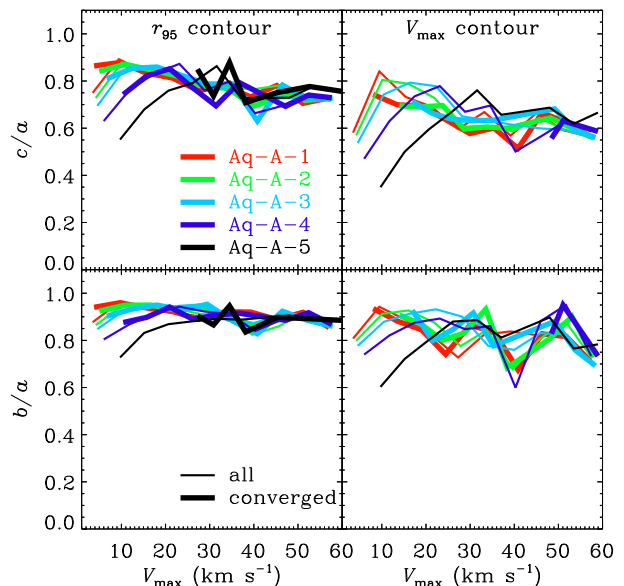


Figure 1. Shape of the r_{95} contour (left) and V_{max} contour (right) as a function of V_{max} for subhalos of the main halo at five different resolutions. With thick lines we plot subhalos for which $r_{\text{conv}} \leq r_{95}$ (left) and $r_{\text{conv}} \leq r_{\text{max}}$ (right), where r_{conv} is such that $\kappa(r_{\text{conv}}) = 7$.

the orbital path of matched objects in different level runs. This is to ensure that the evolution of each subhalo has been comparable in the different resolution runs also in the non-linear regime. More specifically, we define

$$\Delta_{\mathbf{r}}^2 = \frac{1}{N} \sum_{\text{snapshot}} \frac{|\mathbf{r}_3(t) - \mathbf{r}_2(t)|^2}{|\mathbf{r}_2(t)|^2}, \quad (3)$$

with \mathbf{r}_j is the position¹ of the subhalo with respect to the main halo center at the j -th resolution level. This is computed for every snapshot from the time the object is first identified in the simulation box until present day. We consider only structures for which $\Delta_{\mathbf{r}} \leq 0.1$.

A total of 260 substructures are successfully matched in all levels 1,2 and 3 of the Aq-A halo by this procedure. For each object, we define $\delta_s = s_3/s_1 - 1$, where $s = c/a$ measured at r_{max} and the lower indices indicate the resolution level (1 and 3 in the example above). By construction, $\delta_s \sim 0$ for well-converged objects. We show the distribution of δ_s in Fig. 2. The light gray histogram corresponds to all matched objects, and is significantly broader than the distribution for the converged sample (i.e. the subset of the matched sample formed only with the subhalos that have $r_{\text{max}} > r_{\text{conv}}$), which is shown in dark gray.

We illustrate this more clearly on the right panels in Fig. 2, which show the behavior of c/a as a function of radius $R = (abc)^{1/3}$ for three subhalos in the sample. Small colored dots indicate their δ_s value on the histogram on the left. The various curves correspond to the results for different resolution levels as indicated by the labels. For each

¹ The positions of all halos and subhalos are defined by the particle with the minimum potential energy.

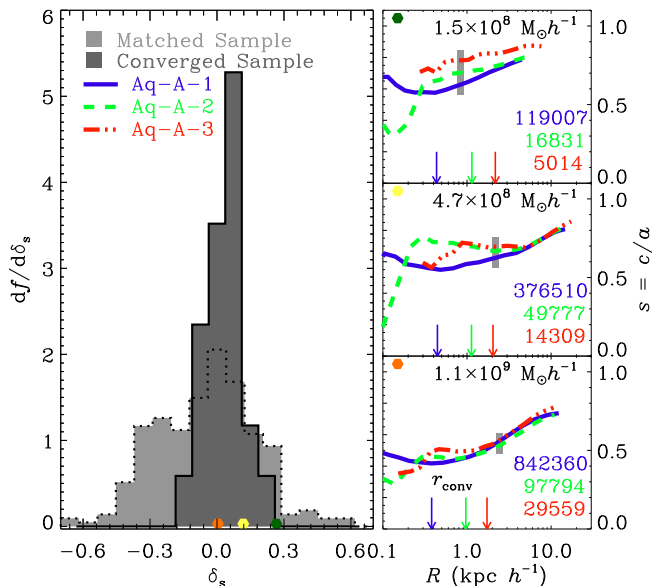


Figure 2. Left: distribution function of the deviation of the major-to-minor axis ratio with respect to the highest resolution simulation δ_s . The light-gray histogram shows the distribution for the matched sample, while the dark-gray shows the results for the sample that satisfies that r_{conv} (vertical arrows in the right panels) is smaller than r_{max} (vertical gray line in the right panels) in all resolutions. The converged sample is narrower by a factor of 5. Right: axis ratios as function of position for three different subhalos with the quoted number of particles in the respective resolutions.

subhalo the convergence radius r_{conv} is marked with a vertical arrow and the position of the V_{max} contour by a vertical thick gray line. The top panel shows a typical example of an unconverged object: the peak of the circular velocity occurs at a smaller radius than r_{conv} for levels 2 and 3. On the other hand, subhalos in the middle and bottom panels have $r_{\text{max}} > r_{\text{conv}}$ and have therefore converged (according to our criterion) at all these levels.

Notice that a large number of particles do not guarantee convergence. For instance, the unconverged object on the top right panel of Fig. 2 has ~ 5000 and ~ 17000 particles in levels 3 and 2, respectively. These are significantly larger than the values previously used in the literature (e.g., Kuhlen, Diemand & Madau 2007; Knebe et al. 2008a,b), and highlights the need to impose a second criterion to measure individual shapes reliably. With our criterion, for only $\sim 2\%$ of the halos with 5000 – 10000 particles have the shapes at the V_{max} contour converged (i.e. $r_{\text{conv}} > r_{\text{max}}$). The situation improves significantly for the r_{95} contour, where 99.6% of such objects have converged.

The distribution of axis ratios for converged objects shown in the left panel of Fig. 2 has a standard deviation $\sigma = 0.08$, meaning that 68.3% of the objects shapes determined at the Aquarius level-3 deviate less than 8% from their value in the highest resolution run. Since we focus on the level-2 runs for the analysis that follows, we expect resolution effects in our sample to be negligible.

The above discussion shows that our criterion for convergence is relatively strict. There are 21403 subhalos with

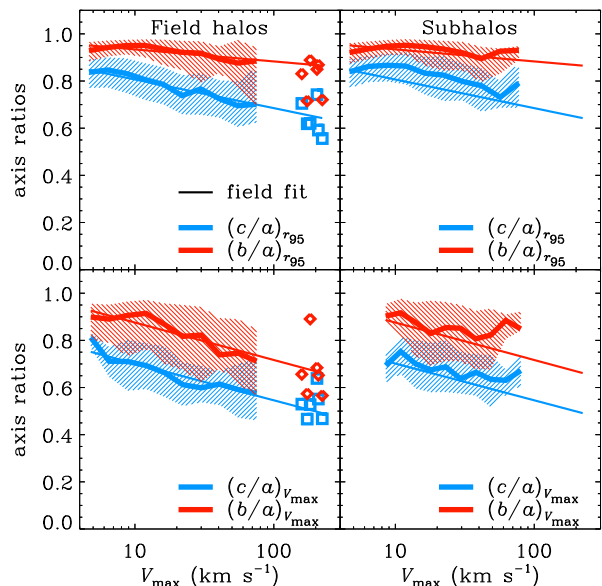


Figure 3. Shape as a function of V_{max} for field halos (left) and subhalos of the main halos in the suite of Aquarius simulations (right). Thick lines represent the median of the distribution of converged structures and the shadowed region represents $\pm 1\sigma$ equivalent dispersion around the median. Thin lines are fits to the objects in the field. The diamonds and squares indicate the axis ratios of the main Aquarius halos.

at least 200 particles within the r_{95} radius in all the Aquarius simulations, and we find that the inertia tensor algorithm converges for 11483 subhalos at the r_{max} contour, and for 13970 at the r_{95} contour. If we now impose our convergence criteria, there remain 412 and 6072 subhalos with well-determined shapes at the r_{max} and r_{95} contours, respectively. For halos in the field our convergence criteria leads to a reduction of 96% and 35% for the r_{max} and r_{95} contours respectively. As expected, there is a larger proportion of field objects whose shapes can be measured at the r_{95} contour. However, despite this significant reduction in sample size, we have gained in the reliability of the shape determination for *individual* halos.

Therefore, in the next section we focus on those halos which satisfy our convergence criteria.

3 HALO SHAPES AS A FUNCTION OF MASS AND ENVIRONMENT

We proceed to characterize the variations in the axis ratios b/a and c/a of dark matter halos according to their mass or, equivalently, their maximum circular velocity. The left column of Fig. 3 shows b/a and c/a for isolated objects measured at the r_{95} radius (labeled r_{95} contour) and at r_{max} (V_{max} contour) in the top and bottom panels, respectively. A thick line indicates the median trend of our sample and the open symbols at the high mass end show the results for the main Aquarius halos from Vera-Ciro et al. (2011). In agreement with previous work, we find that axis ratios tend to decrease gently with V_{max} (Allgood et al. 2006; Macciò et al. 2007; Hahn et al. 2007; Bett et al. 2007; Muñoz-

Cuertas et al. 2011), although we now explore a different mass regime.

Inspection of the top and bottom panels shows that the dependence of the axis ratios with circular velocity is somewhat steeper when measured at r_{\max} than at the r_{95} contours. Typically, our lowest mass objects have inner axes that are rounder by 40 – 50% than those of Milky Way-like halos. Nevertheless, the scatter from object to object at fixed circular velocity also is larger at r_{\max} , as indicated by the shaded regions.

A comparison between the left and the right column of Fig. 3 reveals that there are only small differences between subhalos and isolated objects. To make this comparison easier we overplot in the panels on the right the linear fits obtained for field halos. This shows that, on average, subhalos are slightly more spherical than field halos at a given V_{\max} , but differences are well within the scatter in the samples. The number of converged objects in the case of subhalos is 385 and 1522 for V_{\max} and r_{95} contours, respectively.

Could the differences between field halos and subhalos be caused by measuring shapes at different physical radii? It has been shown in the literature that tidal evolution can significantly decrease r_{\max} in satellites while affecting V_{\max} significantly less (Hayashi et al. 2003; Kravtsov, Gnedin & Klypin 2004; Peñarrubia, Navarro & McConnachie 2008). In that case, the measurement of the halo shape at r_{\max} would be at a smaller radius for a subhalo than for a halo in the field with the same V_{\max} , and the same holds for the r_{95} contour. We address this in Fig. 4, where we show the minor-to-major axis profiles for individual field halos (left) and subhalos (right) of similar mass ($V_{\max} \sim 50 \text{ km s}^{-1}$). The solid dots show the location of r_{\max} for individual objects; they indicate that the radii of the peak circular velocity are comparable in both samples and therefore show that this can not be reason for the different trends reported in Fig. 3. We thus confirm that, on average, subhalos of a given V_{\max} are slightly more spherical than comparable field halos at all radii, particularly in the outskirts. Kolmogorov–Smirnov tests indicate that the difference between both samples is statistically significant only at the r_{95} contours (the Kolmogorov–Smirnov probability is 0.09 in that case versus 0.42 at r_{\max}). However, the differences are well within the object-to-object scatter (see the bottom panel Fig. 4).

The similarity between the subhalo and field populations apparent in Figs 3 and 4 explains the lack of appreciable trends as a function of distance d to the center of the main Aquarius halos, shown in Fig. 5. The typical axis ratios measured at the r_{95} as well as V_{\max} contours do not depend on the distance to the host center up to distances $d \sim 5r_{\text{vir}}$. We have explicitly checked that this is not due to the averaging over random orbital phases of individual subhalos; using the apocenter distances instead of the instantaneous position leads to very similar results. On the other hand, the tidal field of the host seems to imprint a significant radial alignment on the subhalos (see the bottom panel of Fig. 5), which tend to orient their major axis radially to the center of the host, albeit with a large scatter. The signal is stronger close to the center of the main host halos and decreases steadily until it disappears at $d \gtrsim 2r_{\text{vir}}$, where the distribution is consistent with random (Pereira, Bryan & Gill 2008; Pereira & Bryan 2009). Interestingly, inner (at

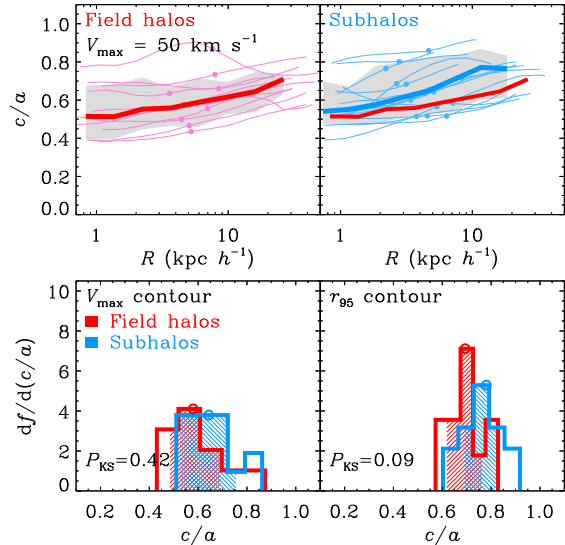


Figure 4. Top: the thin lines show the minor-to-major axis ratio profiles as a function of radius for objects with $V_{\max} \sim 50 \text{ km s}^{-1}$. The thick lines correspond to the median and the shadowed region is 1σ equivalent scatter for the same sample of objects in the field (left) and subhalos (right). The median for field halos is also plotted in the right panel for comparison. Bottom: distribution of the axis ratios of the V_{\max} (left) and r_{95} (right) contour for the field halos (red) and subhalos (blue) plotted in the top panels. Although the median axis ratio (open circle) is slightly larger for subhalos the differences are well within the scatter.

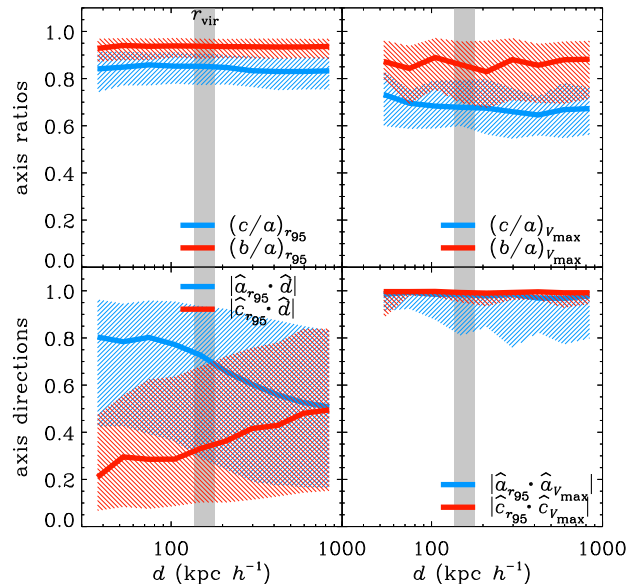


Figure 5. Shape and orientations of subhalos and objects in the field as a function of distance to the main halos d in each of the Aquarius simulations. The gray line indicates the virial radii of the main halos.

Parameter	Median	-1σ	$+1\sigma$
α	0.27	0.07	0.10
r_{-2} (kpc)	1.21	0.42	0.58
v_{-2} (km s $^{-1}$)	9.06	1.87	1.72
c_{Φ}/a_{Φ}	0.70	0.07	0.10
b_{Φ}/a_{Φ}	0.83	0.10	0.09
r_a (kpc)	1.72	1.26	2.86
χ	1.60	0.13	0.09
$\ln A$	-2.42	0.15	0.20

Table 1. Best-fitting values for the profiles shown in Figs. 6 and 8. See text for details.

r_{\max}) and r_{95} contours are well aligned within each object, as shown in the bottom right panel.

Notice that, although our findings suggest only small differences between the shapes of subhalos and field halos, the evolution of *single* objects under the effects of tidal disruption can differ significantly from the behavior of the *population* as a whole (Barber et al., in preparation.) In general, the analysis of a population of subhalos such as that shown in Figs 3–5 will be dominated, in number, by objects with recent infall times (and therefore not largely exposed to tidal effects), minimizing the differences between subhalos and field halos in good agreement with our results.

4 APPLICATION TO THE MODELING OF LOCAL GROUP SATELLITES

As discussed in the Introduction, the Local Group satellite galaxies are expected to inhabit dark matter subhalos comparable to those studied in the previous section. Since the contribution of the baryons to the gravitational potential of these systems is thought to be sub-dominant, the shape, dynamics and orbital structure of their host dark halos may be compared in a reasonably direct way to those of a suitable subset of the subhalos in the Aquarius simulations.

To select subhalos likely to host luminous satellites comparable to local dwarfs we use the semi-analytical model of Starkenburg et al. (2013). The semi-analytic model includes physical prescriptions for the treatment of relevant processes such as radiative cooling, chemical enrichment, star formation, supernova feedback, etc. The parameters in the model are tuned to simultaneously reproduce the luminosity function and spatial clustering of bright galaxies as well as the properties of satellites in the Local Group (De Lucia & Blaizot 2007; De Lucia & Helmi 2008; Li, De Lucia & Helmi 2010).

4.1 The shapes of subhalos hosting luminous satellites

Fig. 6 shows the axis ratios as a function of distance along the major-axis r for our sample of subhalos. This consists of subhalos within the virial radius of their hosts at $z = 0$ and that resemble the *classical satellites* of the Milky Way in their luminosity, i.e. their V -band absolute magnitudes are in the range $-13.2 \leq M_V \leq -8.6$. Each curve is plotted from the convergence radius out to the r_{95} contour, and the color

scale indicates the luminosity assigned by the semi-analytic model to the satellites.

Fig. 6 shows that the dwarf galaxies in the model are surrounded by subhalos that are triaxial, with axis ratios b/a and c/a typically increasing from the inner regions to the r_{95} radius. The scatter from object to object is large, but the overall trend with radius is similar for all subhalos. The median profile, and 1σ -equivalent percentiles of the sample are given, respectively, by the black solid line and the gray shaded area. These dark matter subhalos have on average $c/a \sim 0.60$ and $b/a \sim 0.75$ at a radius of ~ 1 kpc, and turn more spherical close to the r_{95} radius, where $c/a \sim 0.8$ and $b/a \sim 0.9$. Individual inner shapes of halos/subhalos can be clearly seen in Fig. 7, where we show a scatter plot of b/a and c/a ratios measured at $r \sim 1$ kpc. Only converged objects have been included. Different symbols are used for different samples: blue circles for field halos, red diamonds for subhalos and black circles for luminous subhalos. The fact that subhalos and field halos are well mixed in this plane confirms the lack of any significant trend between shape and distance to the main halo, in agreement with Fig. 5.

We may use Poisson’s equation to derive a relation between the b/a and c/a of the density (which our method measures), and those of the potential b_{Φ}/a_{Φ} and c_{Φ}/a_{Φ} . Following Vogelsberger et al. (2008), we introduce a generalized radius:

$$\tilde{r} = \frac{r_a + r}{r_a + r_E} r_E, \quad (4)$$

where $r^2 = x^2 + y^2 + z^2$ is the Euclidean distance, $r_E^2 = (x/a_{\Phi})^2 + (y/b_{\Phi})^2 + (z/c_{\Phi})^2$ is the *ellipsoidal* radius and r_a a characteristic scale. With this definition, $\tilde{r} \approx r_E$ for $r \ll r_a$ and $\tilde{r} \approx r$ for $r \gg r_a$. Assuming that the potential at any point is

$$\Phi(x, y, z) = \tilde{\Phi}(\tilde{r}), \quad (5)$$

where $\tilde{\Phi}$ is the spherically symmetric potential associated with the Einasto profile (Einasto 1965), we find for our sample a median $b_{\Phi}/a_{\Phi} = 0.83$ and $c_{\Phi}/a_{\Phi} = 0.70$. The median and $\pm 1\sigma$ error of the parameter fits for the density and axis ratios obtained in this way are given in Table 1.

4.2 The internal kinematics of subhalos hosting luminous satellites

4.2.1 Behavior along the major axis

Fig. 8 shows the radial velocity dispersion σ_r (top) and the orbital anisotropy β (bottom), both as a function of distance along the major axis. These quantities are computed in ellipsoidal coordinates that follow the axis ratios of the mass density at each radius. In practice, we calculate the component of the velocity in the direction tangential to a given ellipsoid, σ_T , and the radial component σ_r is derived by subtraction in quadrature of σ_T from the total velocity dispersion. Therefore this σ_r corresponds very closely to the velocity dispersion along the spherical radial direction as it is computed along the ellipsoid’s major axis.

As in the previous figure, individual objects are shown with thin lines color-coded according to their V -band absolute magnitude. The median trend of the sample is indicated by a black solid curve, 1σ -equivalent percentiles in

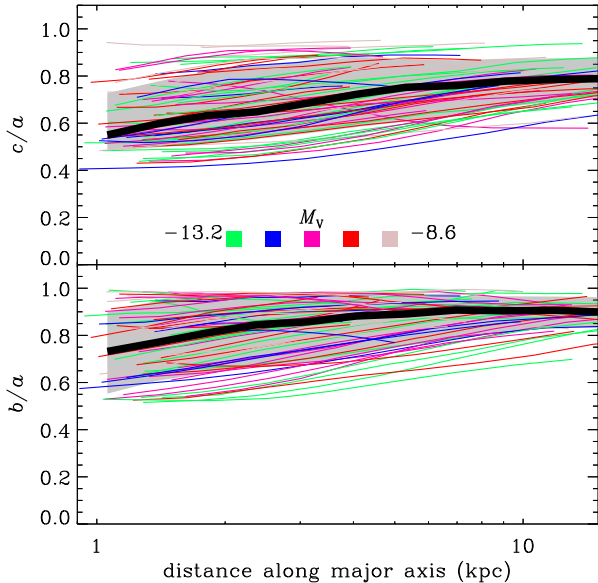


Figure 6. Shape as a function of distance along the major axis, a , for subhalos hosting luminous satellites. The median profile, and 1σ -equivalent percentiles of this sample are given, respectively, by the black solid line and the gray shaded area.

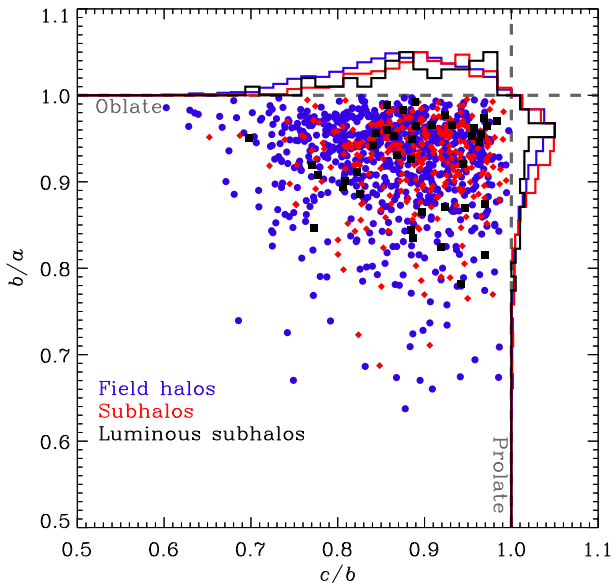


Figure 7. b/a versus c/b axis ratios measured at $r = 1$ kpc for individual (converged) objects. Field halos are shown with blue circles, subhalos with red diamonds and luminous subhalos with black squares. The histograms show that close to the center subhalos may be approximated by oblate axisymmetric objects.

gray shading. The spread in σ_r seen in the top panel of Fig. 8 is due to the difference in mass of the subhalos, which span a range $m = 1.6 \times 10^8 - 5.8 \times 10^9 M_\odot$.

A declining velocity dispersion profile as seen in the top panel of Fig. 8 is generally expected for halos in CDM because of the relation between the density and pseudo phase-

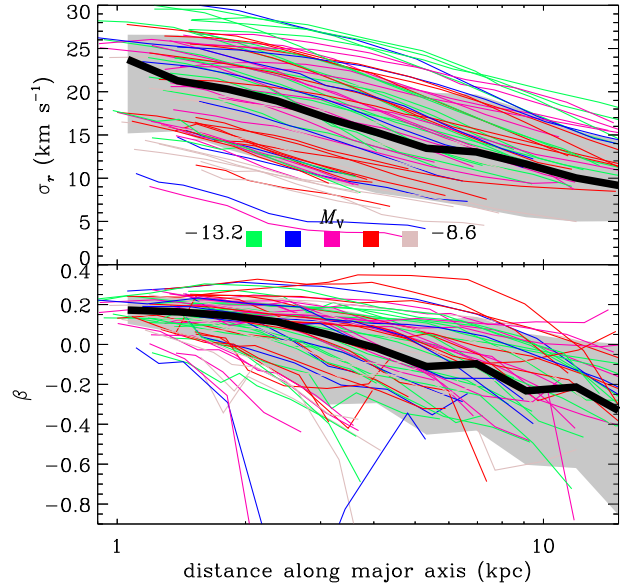


Figure 8. Radial velocity dispersion and anisotropy as a function of the distance along the major axis, r , for the subhalos hosting luminous satellites. The thick solid black line represents the median behavior.

space density, namely $Q = \rho/\sigma_r^3$ (Taylor & Navarro 2001):

$$\frac{\varrho}{\tilde{\sigma}_r^3} = Ax^{-x}, \quad (6)$$

with A a normalization constant, $\varrho \equiv \rho/\rho_{-2}$, $\tilde{\sigma}_r \equiv \sigma_r/v_{-2}$ and $x \equiv r/r_{-2}$, where ρ_{-2} , v_{-2} and r_{-2} are the characteristic density, velocity and radius for the Einasto density profile, respectively². When we fit the Q -profiles individually for each subhalo, we obtain median values of $\ln A = -2.42$ and $\chi = 1.60$, the latter indicating a slightly shallower fall off than for field halos.

In the bottom panel of Fig. 8 we plot the ellipsoidal velocity anisotropy β profiles. Here $\beta = 1 - \sigma_r^2/\sigma_T^2$, where we calculate the component of the velocity tangential and radial to a given ellipsoid as explained above. The velocity anisotropy profiles of dark matter subhalos tend to decline with radius. In the inner regions the motions are slightly radially-biased ($\beta \sim 0.2$ at $r \sim 1$ kpc), while the ellipsoid becomes increasingly tangential ($\beta < 0$) at larger radii. This behavior is markedly different from the radially-biased ellipsoids found in isolated Λ CDM halos, particularly in the outskirts (Cole & Lacey 1996; Taylor & Navarro 2001; Wojtak et al. 2005; Ludlow et al. 2010). This difference is a result of tidal forces, which preferentially remove particles with large apocenters on radial orbits. Fig. 8 also shows that subhalos rarely have a constant β profile.

We may derive an expression for β using the spherical Jeans Equation which relates the density, anisotropy and radial velocity dispersion of a system (Binney & Tremaine 2008). In the case of an Einasto profile with logarithmic

² See Appendix A, where we show that a power-law fit is a reasonable description of the pseudo-phase-space of subhalos just like it is for field halos.

slope $\sim -r^\alpha$ we find:

$$3\beta(r) = -\frac{6\pi\mu}{x\tilde{\sigma}_r^2} + 5x^\alpha - \chi, \quad (7)$$

where $\tilde{\sigma}_r = \sigma_r/v_{-2}$ as before and $\mu = \mu(x, \alpha)$ is given by Eq. (A3) (see Appendix A for a more detailed derivation of this expression). The velocity anisotropy is therefore dependent on the logarithmic slopes of the mass density and of the pseudo phase-space density, α and χ , respectively.

This expression provides a reasonable fit out to $r \sim 2.5r_{-2}$. Whereas the limiting behavior of the anisotropy in the inner regions is similar for all subhalos, beyond a radius of ~ 1 kpc large variations are seen from object-to-object. These variations are still accounted for by Eq. (7) when each β profile is fitted individually. We find that the exact shape of the anisotropy profile depends most strongly on α , while χ determines where the velocity ellipsoid becomes tangential at large radii. On the other hand, variations in $\ln A$ have a very minor effect.

4.2.2 Axisymmetric description of the internal kinematics

Fig. 6 shows that subhalos are not significantly triaxial having in average $b/a \gtrsim 0.8$, therefore, an axisymmetric approach may be sufficient to describe their internal kinematics. Moreover, an oblate approximation seems favoured by the overall distribution of inner shapes shown in Fig. 7, albeit with a large scatter.

To this end, in Fig. 9 we explore the velocity structure in the cylindrical radial and vertical directions. Each object is rotated such that the minor axis coincides with the z -direction. The velocity dispersion components along the vertical (z) and radial (R) axes provide information on how dynamically hot a system is in both directions. We compute this along the two preferential axis, minor (left) and major (right), using at each radius a sphere that contains 400 particles. The velocity dispersion σ_z and σ_R are then computed within these volumes and displayed as a function of distance along the axes. As before, individual halos are shown in thin blue lines, the median values with solid thick lines.

The velocity dispersion profiles show a steady decline with radius, and as expected with a trend similar to the radial velocity dispersion shown in Fig. 6. As in that case, there is scatter from object-to-object mostly due to the range in subhalo mass, with the most luminous objects (light green in Fig. 9) having larger velocity dispersion than the fainter ones (red). The anisotropy β_z is defined as $\beta_z = 1 - \sigma_z^2/\sigma_R^2$ and is shown in the bottom panels of Fig. 9. Interestingly, along the minor axis we find $\sigma_z \sim \sigma_R$, in agreement with the assumptions by Hayashi & Chiba (2012) when modeling stars in the dSph. However, this is not true for the velocity dispersions along the major axis as shown in the right panel, where we find positive values of β_z close to the center and $\beta_z < 0$ at the r_{95} radius. This trend, although systematic, is quite weak, with large scatter amongst the individual objects. It is important to realize that our measurements are subject to significant noise as we are now restricted to consider a small region around a given radius (i.e. we do not average over entire ellipsoidal shells as before and so each sphere contains fewer particles). The typical uncertainty for the individual curves is shown by the black vertical error

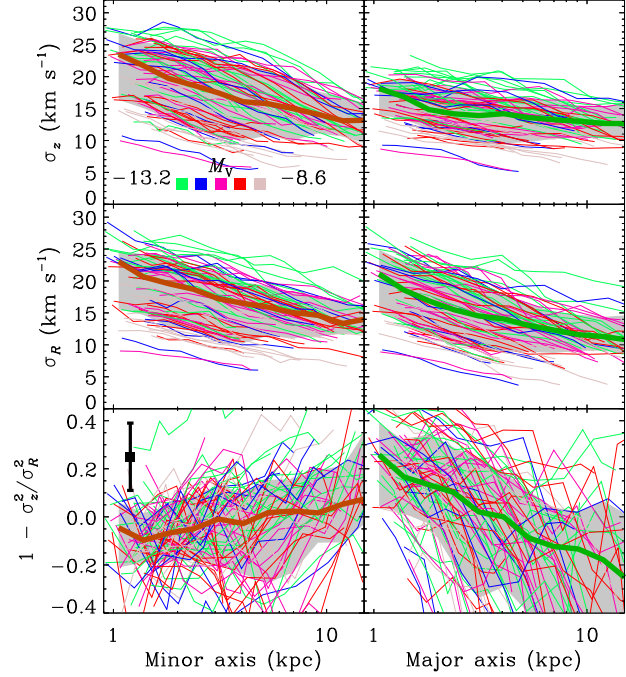


Figure 9. Velocity dispersion as a function of distance along the minor (left) and major axis (right) for subhalos hosting luminous satellites. In each case the system is rotated such that the minor axis lies along the z direction. The cylindrical velocity dispersions σ_z^2 and σ_R^2 are estimated in spheres containing 400 particles.

bar, computed as the dispersion obtained from drawing 100 samples with replacement in each bin.

The fact that the velocity dispersions σ_R and σ_z are not equal implies that the subhalos' distribution functions are a function of a third integral. Although we have shown this to be the case for dark matter satellites, it could also be true for the stars embedded in these systems. Therefore dynamical models of dSph may need to take this into account (Battaglia, Helmi & Breddels 2013), since neglecting this fact can lead to unrealistic estimates of the shapes of the host dark matter halos (see Hayashi & Chiba 2012).

The shapes of the subhalos are consistent with dynamical support by the velocity ellipsoid, as shown by Fig. 10. The vertical axis shows the local anisotropy $\delta = 1 - \sigma_z^2/\sigma_x^2$, where x is again the direction of the major axis and z points along the minor axis. These quantities are calculated in a sphere with 400 particles located at $x = 1$ kpc and the individual points in this figure correspond to the different subhalos. In the axisymmetric case, the virial theorem in tensor form (Binney 2005) gives:

$$\frac{v_0^2}{\sigma_0^2} = 2(1 - \delta) \frac{W_{xx}}{W_{zz}} - 2, \quad (8)$$

where W_{ij} are the components of the potential-energy tensor (Binney & Tremaine 2008). For ellipsoidal systems W_{xx}/W_{zz} is a function of the ellipticity $\epsilon = 1 - c/a$ and is independent of the radial density profile (Roberts 1962). v_0 is the streaming velocity along the y -axis and σ_0 is the velocity dispersion in the x direction. The solid line in Fig. 9 indicates the prediction from Eq. (8) in the case of a dis-

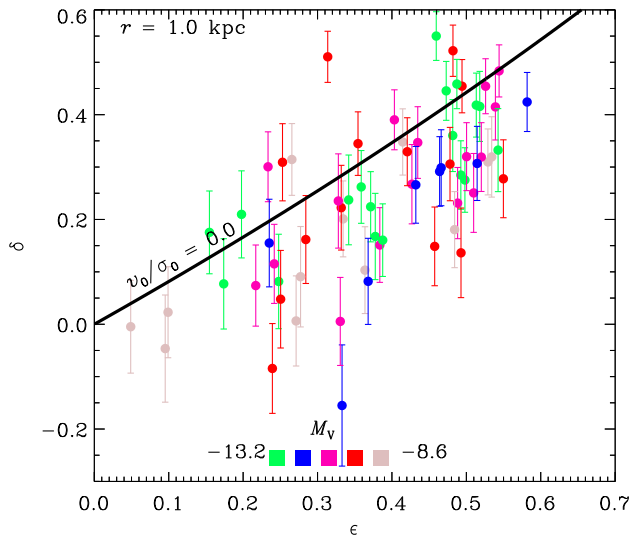


Figure 10. Relation between the anisotropy $\delta = 1 - \sigma_z^2/\sigma_x^2$ and the ellipticity of the halos $\epsilon = 1 - c/a$ measured at a distance $x = 1$ kpc along the major axis. The solid black line shows the prediction of the virial tensor theorem when applied to axisymmetric systems supported by random motion (Binney 2005).

person supported system with $v_0/\sigma_0 = 0$. This prediction provides a reasonable representation of the simulated objects that agrees well with the very little rotation that we find: halos and subhalos show an average $\langle v_0/\sigma_0 \rangle = 0.08$ and more than 90% of the sample has $v_0/\sigma_0 < 0.14$ in their inner regions. The scatter, however, is large and cannot be explained solely on the basis of rotation of subhalos at small radii. Further factors such as departure from axisymmetry or the lack of dynamical equilibrium generated by tides may also contribute to the scatter seen in Fig. 10.

5 CONCLUSIONS

We have used the Aquarius simulations to study the shapes of field and satellite dark matter halos with emphasis on the mass range expected for the hosts of the dwarf galaxies in the Local Group. We have used an iterative method based on the normalized inertia tensor to characterize the principal axis lengths $a \geq b \geq c$ of halos and subhalos as a function of radius. In particular, we have explored in detail halo shapes measured in the inner regions (radius of maximum circular velocity r_{\max}) and in the outskirts or r_{95} contour. Although stars are more centrally concentrated than the dark matter, our resolution allows us to characterize halo shapes at radii as small as $r \sim 1$ kpc, starting to probe the regime traced by the outer stars in dwarf galaxies.

Through a comparison of objects in common between the different resolution levels of the Aquarius simulations, we have noticed that simple number of particles cuts do not guarantee convergence in the measured halo shapes, especially in the inner regions. We find that instead the *convergence radius* r_{conv} (defined as the threshold $\kappa = 7$ in the ratio between the local relaxation time and the dynamical time at the virial radius (Power et al. 2003)) provides a good

estimate of the radius where the axis ratios are robustly determined (with an error $< 8\%$).

We have found that the typical axis ratios of isolated halos in the Aquarius simulations decrease with increasing mass, or equivalently maximum halo circular velocity V_{\max} , i.e. low mass objects tend to be more spherical than Milky Way-like objects. These trends are well approximated by a relation between the axis ratio measured at the r_{95} radius $c/a|_{r_{95}}$ and V_{\max} , i.e. $c/a|_{r_{95}} \sim -0.021 \log V_{\max}$, while this relation is slightly steeper if the axis ratio is measured at r_{\max} contour in which case $c/a|_{r_{\max}} \sim -0.032 \log V_{\max}$. The differences in the shapes of field versus satellite halos are small and within the intrinsic scatter of the samples. Nonetheless, at a fixed V_{\max} , subhalos tend to have larger axis ratios than isolated objects in the field.

The similarity between subhalos and field objects is also apparent in the lack of significant trends in the axis ratios with distance to the main host halo, d . We find, however, that the alignment of the ellipsoids varies with d : dark matter halos at close distances from the host center tend to be oriented preferentially with their major axis pointing radially. The signal disappears only for $d \gtrsim 2.5 r_{\text{vir}}$, where the orientations are consistent with random.

We have also focused on the properties of subhalos likely to host analogs of the *classical satellites* of the Milky Way ($-13.2 \leq M_V \leq -8.6$), according to the semianalytic model of galaxy formation run on the Aquarius suite by Starkenburg et al. (2013). Our analysis indicates that these galaxies are hosted by mildly triaxial dark matter objects with minor-to-major axis ratios $c/a \approx 0.60$ and intermediate-to-major $b/a \approx 0.75$ in the first kiloparsec with a clear trend towards becoming axisymmetric in the outskirts. Their internal orbital structure shows evidence of being affected by tidal forces from their hosts (i.e. the main Aquarius halos), in clear contrast to what is found for isolated systems. We have also found that this orbital structure may be modeled in the axisymmetric context, where the velocity anisotropy $\beta_z \sim 0$ along the minor axis, and declines with distance along the major axis. These results may be used to motivate more realistic models of the subhalos hosting satellite galaxies like those observed around the Milky Way.

ACKNOWLEDGEMENTS

We thank Else Starkenburg for access to the semi-analytical catalog of the Aquarius simulations. AH gratefully acknowledges financial support from the European Research Council under ERC-Starting Grant GALACTICA-240271. The authors thank the hospitality of the Kavli Institute for Theoretical Physics, Santa Barbara during the program “First Galaxies and Faint Dwarfs: Clues to the Small Scale Structure of Cold Dark Matter”, where part of this work was completed under the support of the National Science Foundation Grant No. NSF PHY11-25915. This work was supported in part by the National Science Foundation under Grant No. PHYS-1066293 and the hospitality of the Aspen Center for Physics.

This paper has been typeset from a $\text{\TeX}/\text{\LaTeX}$ file prepared by the author.

REFERENCES

- Abramowitz M., Stegun I. A., 1972, *Handbook of Mathematical Functions*. Dover Publications, New York
- Allgood B., Flores R. A., Primack J. R., Kravtsov A. V., Wechsler R. H., Faltenbacher A., Bullock J. S., 2006, *MNRAS*, 367, 1781
- Amorisco N. C., Evans N. W., 2011, *MNRAS*, 411, 2118
- Amorisco N. C., Evans N. W., 2012, *MNRAS*, 419, 184
- Bailin J., Steinmetz M., 2005, *ApJ*, 627, 647
- Battaglia G., Helmi A., Breddels M., 2013, *New Astron. Rev.*, 57, 52
- Battaglia G., Helmi A., Tolstoy E., Irwin M., Hill V., Jablonka P., 2008, *ApJ*, 681, L13
- Bett P., Eke V., Frenk C. S., Jenkins A., Helly J., Navarro J., 2007, *MNRAS*, 376, 215
- Binney J., 2005, *MNRAS*, 363, 937
- Binney J., Tremaine S., 2008, *Galactic Dynamics: Second Edition*. Princeton University Press, Princeton
- Blumenthal G. R., Faber S. M., Primack J. R., Rees M. J., 1984, *Nat.*, 311, 517
- Boylan-Kolchin M., Bullock J. S., Kaplinghat M., 2012, *MNRAS*, 422, 1203
- Breddels M. A., Helmi A., 2013, *A&A*, 558, A35
- Breddels M. A., Helmi A., van den Bosch R. C. E., van de Ven G., Battaglia G., 2013, *MNRAS*, 433, 3173
- Cole S., Lacey C., 1996, *MNRAS*, 281, 716
- De Lucia G., Blaizot J., 2007, *MNRAS*, 375, 2
- De Lucia G., Helmi A., 2008, *MNRAS*, 391, 14
- Dehnen W., McLaughlin D. E., 2005, *MNRAS*, 363, 1057
- Diemand J., Kuhlen M., Madau P., 2007, *ApJ*, 657, 262
- Diemand J., Kuhlen M., Madau P., Zemp M., Moore B., Potter D., Stadel J., 2008, *Nat.*, 454, 735
- Diemand J., Moore B., 2011, *Adv. Sci. Lett.*, 4, 297
- Dubinski J., Carlberg R. G., 1991, *ApJ*, 378, 496
- Einasto J., 1965, *Trudy Astrofiz. Inst. Alma-Ata*, 5, 87
- Frenk C. S., White S. D. M., Davis M., Efstathiou G., 1988, *ApJ*, 327, 507
- Ghigna S., Moore B., Governato F., Lake G., Quinn T., Stadel J., 1998, *MNRAS*, 300, 146
- Gilmore G., Wilkinson M. I., Wyse R. F. G., Klyna J. T., Koch A., Evans N. W., Grebel E. K., 2007, *ApJ*, 663, 948
- Gott, III J. R., Rees M. J., 1975, *A&A*, 45, 365
- Hahn O., Porciani C., Carollo C. M., Dekel A., 2007, *MNRAS*, 375, 489
- Hansen S. H., Moore B., 2006, *New Astron.*, 11, 333
- Hayashi E., Navarro J. F., Springel V., 2007, *MNRAS*, 377, 50
- Hayashi E., Navarro J. F., Taylor J. E., Stadel J., Quinn T., 2003, *ApJ*, 584, 541
- Hayashi K., Chiba M., 2012, *ApJ*, 755, 145
- Hopkins P. F., Bahcall N. A., Bode P., 2005, *ApJ*, 618, 1
- Jardel J. R., Gebhardt K., 2012, *ApJ*, 746, 89
- Jing Y. P., Suto Y., 2002, *ApJ*, 574, 538
- Kamionkowski M., Koushiappas S. M., Kuhlen M., 2010, *Phys. Rev. D*, 81, 043532
- Kasun S. F., Evrard A. E., 2005, *ApJ*, 629, 781
- Klyna J. T., Wilkinson M. I., Evans N. W., Gilmore G., 2001, *ApJL*, 563, L115
- Klypin A., Gottlöber S., Kravtsov A. V., Khokhlov A. M., 1999a, *ApJ*, 516, 530
- Klypin A., Kravtsov A. V., Valenzuela O., Prada F., 1999b, *ApJ*, 522, 82
- Knebe A., Draganova N., Power C., Yepes G., Hoffman Y., Gottlöber S., Gibson B. K., 2008a, *MNRAS*, 386, L52
- Knebe A., Yahagi H., Kase H., Lewis G., Gibson B. K., 2008b, *MNRAS*, 388, L34
- Kravtsov A. V., Gnedin O. Y., Klypin A. A., 2004, *ApJ*, 609, 482
- Kuhlen M., Diemand J., Madau P., 2007, *ApJ*, 671, 1135
- Li Y.-S., De Lucia G., Helmi A., 2010, *MNRAS*, 401, 2036
- Libeskind N. I., Yepes G., Knebe A., Gottlöber S., Hoffman Y., Knollmann S. R., 2010, *MNRAS*, 401, 1889
- Lokas E. L., 2002, *MNRAS*, 333, 697
- Lokas E. L., 2009, *MNRAS*, 394, L102
- Lokas E. L., Mamon G. A., Prada F., 2005, *MNRAS*, 363, 918
- Long R. J., Mao S., 2010, *MNRAS*, 405, 301
- Ludlow A. D., Navarro J. F., Springel V., Vogelsberger M., Wang J., White S. D. M., Jenkins A., Frenk C. S., 2010, *MNRAS*, 406, 137
- Ludlow A. D., Navarro J. F., White S. D. M., Boylan-Kolchin M., Springel V., Jenkins A., Frenk C. S., 2011, *MNRAS*, 415, 3895
- Macciò A. V., Dutton A. A., van den Bosch F. C., Moore B., Potter D., Stadel J., 2007, *MNRAS*, 378, 55
- Mateo M. L., 1998, *ARA&A*, 36, 435
- Moore B., Ghigna S., Governato F., Lake G., Quinn T., Stadel J., Tozzi P., 1999, *ApJL*, 524, L19
- Muñoz-Cuartas J. C., Macciò A. V., Gottlöber S., Dutton A. A., 2011, *MNRAS*, 411, 584
- Navarro J. F., Frenk C. S., White S. D. M., 1996, *ApJ*, 462, 563
- Navarro J. F., Frenk C. S., White S. D. M., 1997, *ApJ*, 490, 493
- Navarro J. F. et al., 2010, *MNRAS*, 402, 21
- Peñarrubia J., Navarro J. F., McConnachie A. W., 2008, *ApJ*, 673, 226
- Pereira M., Bryan G. L., 2009, in *Bulletin of the American Astronomical Society*, Vol. 41, American Astronomical Society Meeting Abstracts #213, p. 315.03
- Pereira M. J., Bryan G. L., Gill S. P. D., 2008, *ApJ*, 672, 825
- Power C., Navarro J. F., Jenkins A., Frenk C. S., White S. D. M., Springel V., Stadel J., Quinn T., 2003, *MNRAS*, 338, 14
- Press W. H., Schechter P., 1974, *ApJ*, 187, 425
- Richstone D. O., Tremaine S., 1986, *AJ*, 92, 72
- Roberts P. H., 1962, *ApJ*, 136, 1108
- Schneider M. D., Frenk C. S., Cole S., 2012, *J. Cosmol. Astropart. Phys.*, 5, 30
- Springel V. et al., 2008, *MNRAS*, 391, 1685
- Springel V., White S. D. M., Tormen G., Kauffmann G., 2001, *MNRAS*, 328, 726
- Stadel J., Potter D., Moore B., Diemand J., Madau P., Zemp M., Kuhlen M., Quilis V., 2009, *MNRAS*, 398, L21
- Starkenburger E. et al., 2013, *MNRAS*, 429, 725
- Stoehr F., White S. D. M., Tormen G., Springel V., 2002, *MNRAS*, 335, L84
- Strigari L. E., Bullock J. S., Kaplinghat M., Diemand J., Kuhlen M., Madau P., 2007, *ApJ*, 669, 676
- Strigari L. E., Bullock J. S., Kaplinghat M., Simon J. D., Geha M., Willman B., Walker M. G., 2008, *Nat.*, 454, 1096

- Strigari L. E., Frenk C. S., White S. D. M., 2010, MNRAS, 408, 2364
- Taylor J. E., Navarro J. F., 2001, ApJ, 563, 483
- Thomas P. A. et al., 1998, MNRAS, 296, 1061
- Tormen G., 1997, MNRAS, 290, 411
- Tormen G., Diaferio A., Syer D., 1998, MNRAS, 299, 728
- Vera-Ciro C. A., Helmi A., Starkenburg E., Breddels M. A., 2013, MNRAS, 428, 1696
- Vera-Ciro C. A., Sales L. V., Helmi A., Frenk C. S., Navarro J. F., Springel V., Vogelsberger M., White S. D. M., 2011, MNRAS, 416, 1377
- Vogelsberger M., White S. D. M., Helmi A., Springel V., 2008, MNRAS, 385, 236
- Walker M., 2013, Dark Matter in the Galactic Dwarf Spheroidal Satellites, Springer Netherlands, p. 1039
- Walker M. G., Mateo M., Olszewski E. W., Peñarrubia J., Wyn Evans N., Gilmore G., 2009, ApJ, 704, 1274
- Walker M. G., Peñarrubia J., 2011, ApJ, 742, 20
- Warren M. S., Quinn P. J., Salmon J. K., Zurek W. H., 1992, ApJ, 399, 405
- White S. D. M., Rees M. J., 1978, MNRAS, 183, 341
- Wilkinson M. I., Kleyna J., Evans N. W., Gilmore G., 2002, MNRAS, 330, 778
- Wojtak R., Lokas E. L., Gottlöber S., Mamon G. A., 2005, MNRAS, 361, L1
- Wolf J., Martinez G. D., Bullock J. S., Kaplinghat M., Geha M., Muñoz R. R., Simon J. D., Avedo F. F., 2010, MNRAS, 406, 1220

APPENDIX A: EINASTO PROFILES AND THE SPHERICAL JEANS EQUATION

Following the method of Vera-Ciro et al. (2013) we fit a Einasto profile to the circular velocity profile of each individual subhalo of our sample. For each object we take 20 bins equally spaced in logarithmic space between $r_{\text{conv}} < r < 0.9r_{95}$. We compute the cumulative circular velocity profile and fit an Einasto model by minimizing the merit function $E = \sum_{i=1}^{N_{\text{bins}}} (\ln v_c^2(r_i) - \ln v_{c,i}^2)^2 / N_{\text{bins}}$ against the free parameters r_{-2} , ρ_{-2} and α . Here, $v_{c,i}$ is the circular velocity corresponding to an Einasto profile with a scale radius r_{-2} (the radius at which the density profile has a slope -2), a characteristic density at r_{-2} equal to ρ_{-2} and a shape parameter that controls the overall slope of the profile, α . We deliberately chose the circular velocity profile over the more widely used density profile which is more sensitive to shot noise in each bin (see Vera-Ciro et al. 2013, for more details).

The density profile can be written as,

$$\rho(r) = \rho_{-2} \varrho(r/r_{-2}), \quad (\text{A1})$$

where

$$\ln \varrho(x) = -\frac{2}{\alpha} (x^\alpha - 1). \quad (\text{A2})$$

ϱ is therefore a dimensionless function of the dimensionless variable $x = r/r_{-2}$. In this spirit, it is possible to define a set of scaling factors in which we can express the dynamics of the system, namely, a characteristic mass $m_{-2} \equiv r_{-2}^3 \rho_{-2}$ and characteristic velocity $v_{-2} \equiv G r_{-2}^2 \rho_{-2}$ [note that v_{-2}

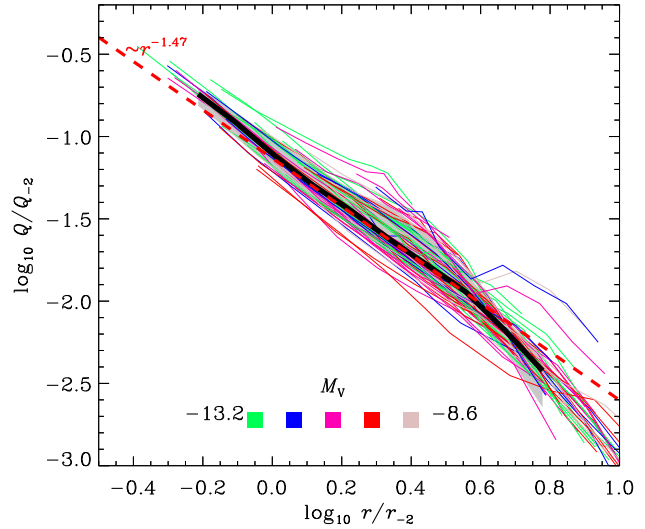


Figure A1. Pseudo-phase-space density profile $Q/Q_{-2} = \varrho/\tilde{\sigma}_r^3$ for the subhalos hosting luminous dwarfs in our sample. The black line shows the mean profile of all subhalos and the red curve indicates the best power law fit $Q \sim r^{-1.47}$.

is not $v_{\text{circ}}(r_{-2})$]. The enclosed mass within a radius r is therefore $m(r) = 4\pi m_{-2} \mu(r/r_{-2})$, where

$$\begin{aligned} \mu(x) &= \int_0^x dx x^2 \varrho(x) \\ &= \frac{1}{\alpha} \exp\left(\frac{3 \ln \alpha + 2 - \ln 8}{\alpha}\right) \gamma\left(\frac{3}{\alpha}, \frac{2x^\alpha}{\alpha}\right), \quad (\text{A3}) \end{aligned}$$

with γ the lower incomplete gamma function. In a similar fashion we can define a dimensionless version of the radial velocity dispersion $\tilde{\sigma}_r(x) \equiv \sigma_r(r_{-2}x)/v_{-2}$.

It has been previously reported in the literature that the pseudo phase-space density profile of isolated dark matter halos can be well modeled by a single power law $Q \equiv \rho/\sigma_r^2 \sim r^{-\chi}$, $\chi > 0$ (Taylor & Navarro 2001; Dehnen & McLaughlin 2005; Navarro et al. 2010; Ludlow et al. 2011). Fig. A1 shows Q measured for our sample of subhalos hosting luminous satellites. We have found that the slope χ is slightly shallower than for objects in the field ($\chi \sim 1.6$ versus $\chi \sim 1.8$ for isolated halos). The best-fitting values of the parameters, and their variance, are given in Table 1.

Notice that the pseudo-phase-space profiles start to deviate from a power-law in the outer regions, likely induced by ongoing tidal stripping. This typically occurs for $\log r/r_{-2} \geq 0.6$, which is roughly the same scale at which our fit for the radial velocity dispersion σ_r deviates from the mean subhalo trends shown in Fig. 8.

Using the dimensionless quantities introduced before, we can now write the spherical Jeans equation as:

$$\begin{aligned} \frac{d}{dx} (\varrho \tilde{\sigma}_r^2) + 2 \frac{\beta}{x} (\varrho \tilde{\sigma}_r^2) &= -\frac{4\pi \varrho \mu}{x^2} \\ \Rightarrow \frac{d \ln \varrho}{d \ln x} + 2 \frac{d \ln \tilde{\sigma}_r}{d \ln x} + 2\beta &= -\frac{4\pi \mu}{x \tilde{\sigma}_r^2}. \quad (\text{A4}) \end{aligned}$$

We can use Eq. (A2) to further reduce this expression:

$$3\beta(x) = -\frac{6\pi \mu}{x \tilde{\sigma}_r^2} + 5x^\alpha - \chi. \quad (\text{A5})$$

The limiting value of this expression at small radii can be obtained from a Taylor expansion around zero. For $x \ll 1$ we may use that $\lim_{x \rightarrow 0} \gamma(s, x)/x^s = 1/s$ (Abramowitz & Stegun 1972). Finally

$$\begin{aligned} \ln \varrho(x) &\approx \frac{2}{\alpha}, \\ \mu(x) &\approx \frac{1}{3} x^3 e^{2/\alpha}, \\ \tilde{\sigma}_r(x) &\approx A^{-1/3} e^{2/3\alpha} x^{\chi/3}, \quad x \ll 1, \end{aligned}$$

which leads to

$$3\beta(x) \approx -2\pi A^{2/3} e^{2/3\alpha} x^{2(1-\chi/3)} + 5x^\alpha - \chi, \quad x \ll 1. \quad (\text{A6})$$